Marko Mikulec
Henry Piehl

http://dx.doi.org/10.21278/brod74103

ISSN 0007-215X
eISSN 1845-5859

Verification and validation of CFD simulations with full-scale ship speed/power trial data

UDC 629.5.016:629.5.018.75:004.415.5
Original scientific paper

Summary

Verification and validation of Computational Fluid Dynamics (CFD) simulations of a full-scale ship trial are presented in this study. Speed/power trials were carried out according to industry standards for three different power settings. Measured data was corrected for environmental effects to obtain ideal trial runs. Ship-scale unsteady RANS CFD simulations were conducted. Grid refinement sensitivity was evaluated for each power setting. Furthermore, time-step sensitivity was assessed for the selected grids. Finally, assumptions regarding symmetry condition and turbulence model were verified. Simulated results were in good agreement with the test data, thus illustrating the capabilities of numerical methods to determine ship performance at full scale.

Keywords: *Computational Fluid Dynamics; full-scale; speed/power trial; sea trial; self-propulsion; verification; validation*

1. Introduction

Supported by the advancements in computational science, engineers can run more and more complex Computational Fluid Dynamics (CFD) simulations. However, to use the results from these simulations with confidence, accuracy and uncertainty must be assessed through verification and validation. There are established methods based on Richardson extrapolation for verification of marine CFD simulations, such as the Grid Convergence Index (GCI) method presented in [1]. On the other hand, to validate simulation results, real measurements are required. Due to the scarcity of ship-scale test data, researchers commonly rely on model-scale experiments in towing tanks. This, however, introduces scaling issues, as Reynolds equality is violated. Additionally, these experiments are costly and time-consuming. Furthermore, different flow conditions between full and model scale in the propeller region contribute to the problematic nature of extrapolation self-propulsion results to ship scale. These well-known issues are addressed for conventional ships using extrapolation procedures such as the 1978 ITTC Performance Prediction method described in [2]. These methods are based on years of experience and collected data. Still, in some cases, scale effects can cause a more profound difference between model and full-scale performance, which renders standard extrapolation procedures unsuitable. In their work, Hochkirch and Mallol outlined relatively

thinner boundary layer in full-scale, delayed flow separation and vortex formation and potential changes in the wave pattern in the stern region in full-scale flows as main scale effects [3]. Since propulsion devices partially operate in the boundary layer, it is only natural that they behave differently in model and full-scale. Scale effects have been investigated using CFD by Castro et al. [4]. After conducting both model and full-scale self-propulsion simulations for the KCS case, the authors concluded that the thinner boundary layer in full-scale improves propeller performance as the propeller is subject to more uniform velocities. Furthermore, due to more profound viscous effects, different wave elevation at the stern and in the wake was observed in full-scale. Farkas et al. came to a similar conclusion in their investigation of the nominal wake for a handymax bulk carrier and pointed out the benefits of the full-scale numerical simulations [5]. A numerical study of the flow around the Japan Bulk Carrier with and without an energy saving device was carried out by Visonneau et al. [6]. The authors observed significantly different flow characteristics in the stern region when comparing model-scale and full-scale simulations. They thus concluded that full-scale CFD simulations should be a part of the design process for such devices. In their work, Farkas et al. conducted an extensive numerical and experimental assessment of the hydrodynamic characteristics of a bulk carrier [7]. Self-propulsion and resistance results were extrapolated to full scale using five different extrapolation methods. Results were then compared with full-scale CFD simulation, highlighting the importance of CFD in the investigation of scale effects but also voicing the need for validation based on full-scale measurements.

The problem of extrapolation from a model scale to a ship scale can be avoided using full-scale CFD simulations [8]. With that in mind, there is an ongoing effort in research to validate full-scale CFD simulations directly against sea trial measurements. Lloyd's Register hosted the first workshop on full-scale hydrodynamic simulations, where participants had access to sea trial measurements for a general cargo vessel [9]. Based on full-scale measurements, Ponkratov and Zegos validated full-scale self-propulsion CFD simulations for a medium-range tanker, showing promising results [10]. The values obtained from simulations had better agreement with the measured data than those based on the ITTC78 performance prediction method. In another study, Jasak et al. validated full-scale simulations with sea trial data for a general cargo carrier and a car carrier [11]. For both cases, the CFD results were in very good agreement with the measured data. Recently, Orych et al. performed verification and validation of CFD simulations at full scale for a single screw cargo vessel [12]. Validation was based on sea trial data, and computed results were in good agreement with measurements.

The principal goal of this study is to simulate a self-propelled vessel at different velocities and validate obtained global characteristics (e.g., propeller revolutions) against sea trial measurements. For this, a speed/power sea trial was conducted using the Research Vessel Gunnerus, owned by the Norwegian University of Science and Technology. Two double runs were performed for three different power settings during the trial. Data obtained from the trial was analysed and corrected according to ITTC procedures [13]. Three sets of ship-scale self-propulsion CFD cases were set up based on the Reynolds-averaged Navier-Stokes equations for a transient, incompressible, free surface flow. As demonstrated by Degiuli et al., the turbulence model is not expected to have a significant impact on the total resistance [14]. Therefore, the two-equation $k-\varepsilon$ turbulence model was used for turbulence modelling, as it is more economical in terms of processing power than the $SST\ k-\omega$ model [15]. The Volume of Fluid method was used to capture the free surface. To reduce the required computational effort, azimuth thrusters were modelled using the virtual disk method. In addition to a mesh study, the time-step sensitivity was investigated to verify the simulation setup. The simulation results were validated against the corrected sea trial measurements.

The paper is organized as follows. First, the details regarding planning, execution, and analysis of results from the sea trial are presented. Then, the mathematical and numerical modelling is addressed, outlining the methods used in setting up the CFD simulations. Next, verification results are presented, including azimuth open water simulations and grid and time-step sensitivity studies for self-propulsion cases. Further, assumption regarding the selection of the turbulence model and the use of symmetry boundary condition are addressed. The findings are summarized and discussed at the end.

2. Sea trial

2.1 RV Gunnerus

Research Vessel Gunnerus, Fig. 1 and Fig. 2, is equipped with cutting-edge technology and sensors for various research activities and provides an invaluable platform for educational purposes. All available sensor data is logged with a 1 Hz frequency. The ship's principal particulars are listed in Table 1.

Fig. 1 RV Gunnerus (bow view)

Fig. 2 RV Gunnerus (stern view)

Table 1 Gunnerus principal particulars

Length between perpendiculars	L_{PP}, m	33.90
Breadth moulded	B, m	9.60
Draught moulded	T, m	2.70
Depth to first deck	D, m	4.28
Block coefficient	C_B	0.59
Displacement	Δ, tons	555.75
Longitudinal centre of gravity	LCG, m	15.13
Vertical centre of gravity	VCG, m	3.40
Pitch radius of gyration	r_{yy}, m	$0.25L_{PP}$
Propeller diameter	$D_{P,\,\mathrm{m}}$	1.90
Number of blades	N	4

The vessel is equipped with two permanent magnet driven azimuth thrusters with a distinctive propeller design, as shown in Fig. 3. The propellers are both rotating inwards, i.e., they are counter-rotating. Shortly before the trial, the vessel was dry-docked, during which both hull and azimuths were thoroughly cleaned of marine growth. Unfortunately, the surface roughness has not been measured.

Fig. 3 RV Gunnerus main propulsors

2.2 Sea trial description

The sea trial was planned and conducted following the ITTC guidelines for speed/power tests [13]. Due to technical limitations, the maximum available power setting was 77% on the day of the trial. Therefore, the tested power settings were 77%, 60% and 40% of the maximum power. Two double runs were carried out for each power setting to account for the sea current influence. A single double-run consists of two runs with reciprocal heading over the same ground area. The trial was executed in a sheltered area to minimize the effects of environmental conditions such as wind and waves. Furthermore, all runs were conducted in deep water. On average, observed weather conditions were between Beaufort 2 and 3, as shown in Fig. 4. The course was kept constant by the auto-pilot according to the planned trial routes. Minimum steering input was registered, as thruster toe angles never exceeded 2° across all trial runs. GPS tracks of all runs are shown in Fig. 5.

Fig. 4 Trial conditions

Fig. 5 GPS tracks for all trial runs

2.3 Sea trial results

The measured data included vessel speed over ground, GPS position, relative wind speed and direction, propeller revolutions and delivered power. Due to the nature of the propulsion system, the delivered power was not directly measured on the shaft but calculated according to the power plant manufacturer's specifications. Wave conditions were derived from visual observation by experienced seamen on board, as the wave radar was not correctly calibrated. ITTC procedures and guidelines as presented in [13], were followed during the analysis of the collected data. Therefore, the detailed procedure is omitted, and only the final results are presented.

For each power setting, a single ship's speed through the water is calculated using the 'Mean of means' method, under the assumption that the velocity of the sea current changes parabolically over time. The Direct Power Method is used to correct measured power and propeller revolutions. As the name implies, measured power is directly adjusted for the power increase due to the added resistance in the trial conditions. The usual ITTC procedure includes calculating the added resistance due to wind, waves, water temperature and density, water depth and displacement (if the trial displacement is different from the agreed one). In this case, however, simulations are set up using the water properties and loading case encountered on the day of the trial since the trial was performed for research purposes. Therefore, only corrections for wind and waves were made. The trial was conducted in relatively deep water; hence no correction is needed for the shallow water effects.

2.3.1 Added resistance due to wind

The measured relative wind speed and direction are first averaged over the duration of each run. The true wind vector is derived for all runs based on the ship's heading and speed over the ground. By averaging true wind vectors obtained for each run in a set, the true wind vector is found for a single power setting. Finally, based on the obtained true wind vector for a set of runs, corrected relative wind is recalculated for each run.

To calculate the resistance increase due to wind, ship's wind resistance coefficients are necessary. These coefficients can be obtained from a wind tunnel test, CFD simulations or regression models. Since these models are based on data collected from large commercial vessels, they are not applicable to RV Gunnerus. Further, wind tunnel test data is not

available, so the only viable alternative to obtain wind resistance coefficients was also to use CFD simulations.

A set of steady state, single phase, RANS CFD simulations were set up with a simplified ship geometry above the water line level. Since the superstructure is not symmetric, coefficients are obtained for 360° around the vessel, with 15° increments. The simulations were run at full scale with approximately 12 million cells. The uncertainty due to grid refinement and other parameters was not quantified in this case. Simulation results are shown in Fig. 6, with 0º being the headwind.

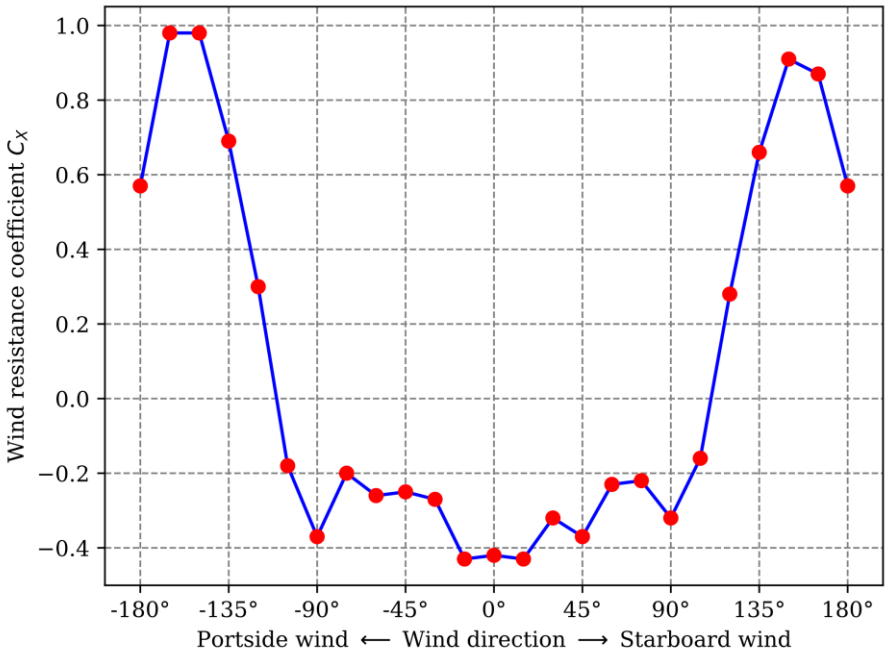

Fig. 6 Wind resistance coefficients

2.3.2 Added resistance due to waves

Since mild sea states with relatively low wave heights were encountered during the trials, the simplified method STAWAVE-1 developed by STA-JIP [16] was used to estimate the wave resistance. The method assumes that the wave-induced motion can be neglected and only accounts for added resistance from wave reflections of the hull on the waterline. It is applicable for head waves within ±45°off the bow. No correction is applied for waves outside this range.

2.3.3 Measured and corrected results

As previously mentioned, all relevant values are averaged over each single run at a particular power setting. Delivered power and propeller revolutions are corrected for all runs separately. Due to the complexity of the propulsion devices, propeller overload test results are unavailable. Therefore, the overload factor for power correction is neglected. For correcting propeller revolutions, a tentative value of 0.2 is used for the overload factor, as used in STAIMO, software developed by STA-Group for analysing speed/power trial measurements [17]. Furthermore, the propulsive efficiency coefficient is obtained from model tests conducted by SINTEF for using a similar propulsion unit. Measured and corrected values for 77%, 60% and 40% maximum power are presented in Table 2, Table 3 and Table 4, respectively. Finally, these values are averaged over each run-set to obtain a single measured and corrected value for each power setting which can then be compared with the simulation

results. The final corrected values represent the ideal runs from which all environmental effects such as wind and waves have been deducted. These values, alongside the difference between corrected and measured results, are presented in Table 5.

Table 2 Measured and corrected results for runs at 77% power

77% Power	Measured			Corrected		
Run nr.	V_G, kn	$P_{D,m}$, kW	n_m, min^{-1}	V_S, kn	$P_{D,corr}$, kW	n_{corr}, min^{-1}
1	10.85	534.22	164.18	10.53	541.73	164.65
2	10.24	539.83	164.24		509.58	162.32
3	10.80	535.20	164.19		539.97	164.48
4	10.25	540.59	164.22		508.98	162.21

Table 3 Measured and corrected results for runs at 60% power

60% Power	Measured			Corrected		
Run nr.	V_G, kn	$P_{D,m}$, kW	n_m, min^{-1}	V_S, kn	$P_{D,corr}$, kW	n_{corr}, min^{-1}
1	8.50	247.41	126.71	8.46	236.90	125.60
2	8.40	249.87	127.08		245.57	126.64
3	8.51	248.16	126.98		243.13	126.46
4	8.43	248.01	126.97		240.68	126.21

Table 4 Measured and corrected results for runs at 40% power

40% Power	Measured			Corrected		
Run nr.	V_G, kn	$P_{D,m}$, kW	n_m, min^{-1}	V_S, kn	$P_{D,corr}$, kW	n_{corr}, min^{-1}
1	4.97	54.19	73.62	5.02	49.84	72.36
2	5.09	52.07	73.57		50.78	73.20
3	4.95	54.32	73.64		49.48	72.23
4	5.07	52.26	73.62		49.66	72.86

Table 5 Measured and corrected ideal runs

	Measured		Corrected		Difference	
V_S, kn	$P_{D,m}$, kW	n_m, min^{-1}	$P_{D,corr}$, kW	n_{corr}, min^{-1}	ΔP_D, %	Δn, %
10.53	537.46	164.21	525.07	163.42	-2.31	-0.49
8.46	248.37	126.94	241.57	126.23	-2.74	-0.56
5.02	53.21	73.62	49.94	72.7	-6.15	-1.30

3. Mathematical and numerical modelling

3.1 Governing equations

When considering incompressible flows, without the presence of body forces, the averaged continuity and momentum equations can be expressed in tensor notation and Cartesian coordinates in the following form [18]:

$$\frac{\partial(\rho\bar{u}_i)}{\partial x_i} = 0 \tag{1}$$

$$\frac{\partial(\rho\bar{u}_i)}{\partial t}+\frac{\partial}{\partial x_j}\left(\rho\bar{u}_i\bar{u}_j+\rho\overline{u_i'u_j'}\right)=\frac{\partial\bar{p}}{\partial x_i}+\frac{\partial\bar{\tau}_{ij}}{\partial x_j} \tag{2}$$

Where ρ is density of the fluid, $\bar{u}_i$ is the averaged velocity component, $\overline{u_i'u_j'}$ is the Reynolds stress term and p is the mean pressure. Finally, $\bar{\tau}_{ij}$ is the mean viscous stress tensor which is expressed as:

$$\bar{\tau}_{ij}=\mu\left(\frac{\partial\bar{u}_i}{\partial x_j}+\frac{\partial\bar{u}_j}{\partial x_i}\right) \tag{3}$$

To form a closed system of equations, a turbulence model is used in conjunction with equations (1) and (2). For this purpose, a Realizable Two-Layer $k-\varepsilon$ turbulence model is used. Transport equations for the kinetic energy k and the turbulent dissipation rate ε are introduced, as described in [19]:

$$\frac{\partial}{\partial t}(\rho k)+\nabla\cdot(\rho k\bar{\mathbf{v}})=\nabla\cdot\left[\left(\mu+\frac{\mu_t}{\sigma_k}\right)\nabla k\right]+P_k-\rho(\varepsilon-\varepsilon_0)+S_k \tag{4}$$

$$\frac{\partial}{\partial t}(\rho\varepsilon)+\nabla\cdot(\rho\varepsilon\bar{\mathbf{v}})=\nabla\cdot\left[\left(\mu+\frac{\mu_t}{\sigma_\varepsilon}\right)\nabla\varepsilon\right]+\frac{1}{T_e}C_{\varepsilon1}P_\varepsilon-C_{\varepsilon2}f_2\rho\left(\frac{\varepsilon}{T_e}-\frac{\varepsilon_0}{T_0}\right)+S_\varepsilon \tag{5}$$

Where $\bar{\mathbf{v}}$ is the mean velocity, μ is the dynamic viscosity, σ_k, σ_ε, $C_{\varepsilon1}$ and$C_{\varepsilon2}$ are model coefficients, P_k and P_ε are production terms, f_2 is a damping function, S_k and S_ε are the user-specified source terms, ε_0 is the ambient turbulence value and T_0 is the specific time-scale for an ambient source term.

To capture interface between the two phases, Volume of Fluid (VoF) method is used, as described in [19]. In this method, the distribution of phases and the position of the interface between them are described by phase volume fraction α_i. The volume fraction of an individual phase i is defined as:

$$\alpha_i=\frac{V_i}{V} \tag{6}$$

Where V_i is the volume of phase i, and V the cell volume. Naturally, the sum of all phases in a cell must be equal to one:

$$\sum_{i=1}^{N}\alpha_i=1 \tag{7}$$

Where N is the total number of phases. Depending on the volume fraction, a cell can be completely filled with phase i ($\alpha_i=1$) or completely free of phase i ($\alpha_i=0$). Values between these two extremes indicate that an interface is present in the cell. Since the method is unable to distinguish the exact position of a certain phase within the cell, a fine mesh resolution is necessary to properly resolve the interface.

In azimuth open water simulations, Moving Reference Frame (MRF) method was used to emulate propeller rotation. MRF uses a concept of a reference frame which translates and rotates with respect to a fixed reference frame in the domain. Since a time-resolved solution is not required, this approach enables modelling of the propeller rotation as a steady-state

problem, by keeping the mesh stationary. The velocity of a material point P with respect to the moving reference frame (i.e., relative velocity) can be written as [19]:

$$\mathbf{v}_r = \mathbf{v} - \mathbf{v}_{MRF,t} - \boldsymbol{\omega}_{MRF} \times \mathbf{r}_{P,MRF} \tag{8}$$

Where $\mathbf{v}$ is the velocity in the fixed reference frame (i.e., absolute velocity), $\mathbf{v}_{MRF,t}$ is the velocity of the moving reference frame origin with respect to the fixed frame, $\boldsymbol{\omega}_{MRF}$ is the angular velocity of the moving reference frame with respect to the fixed frame and $\mathbf{r}_{P,MRF}$ is the position vector of the material point with respect to the moving reference frame.

In self-propulsion simulations, the body force propeller is used to model the azimuth thrusters. This method significantly reduces computational costs, as the propeller and nozzle geometries are not discretized. Instead, volumetric source terms are introduced in a virtual disk region which replaces the propeller. These terms vary in the radial direction according to the Goldstein principle [20], and they are implemented in the following manner [19]:

$$f_{bx} = A_x r^* \sqrt{1 - r^*} \tag{9}$$

$$f_{b\theta} = A_\theta \frac{r^* \sqrt{1 - r^*}}{r^*(1 - r_h') + r_h'} \tag{10}$$

$$r^* = \frac{r' - r_h'}{1 - r_h'} \tag{11}$$

$$r_h' = \frac{R_H}{R_P} \tag{12}$$

$$r' = \frac{r}{R_P} \tag{13}$$

Where f_{bx} and $f_{b\theta}$ are axial and tangential body force components, r is the radial coordinate, R_H is the hub radius and R_P is the propeller tip radius. The constants A_x and A_θ are calculated as:

$$A_x = \frac{105}{8} \frac{T}{\pi \Delta (3R_H + 4R_P)(R_P - R_H)} \tag{14}$$

$$A_\theta = \frac{105}{8} \frac{Q}{\pi \Delta R_P (3R_H + 4R_P)(R_P - R_H)} \tag{15}$$

Where T is the propeller thrust, Q is the propeller torque, and Δ is thickness of the virtual disk. In addition to the propeller open water efficiency η_0, dimensionless thrust and torque coefficients K_T and K_Q as functions of the propeller advance ratio J are required as an input. Since the whole azimuth unit was replaced with a virtual disk, the induced velocity correction was not applied, as it would introduce additional uncertainties in this case.

3.2 Numerical setup

Numerical simulations are conducted using the commercial software package STAR-CCM+. The Finite Volume Method (FVM), as described in [18], is used for spatial discretization of the governing equations. A first-order implicit Euler scheme is used for temporal discretization [21], and a second-order upwind scheme is used for the convection terms [22].

The so-called Dynamic Fluid Body Interaction (DFBI) method is used to model heave and pitch motion while all other degrees of freedom are kept fixed. The ship is moved iteratively until equilibrium position is achieved, i.e., until forces and moments acting on the body are in balance for the selected degrees of freedom. Since the surge motion is fixed, the self-propulsion point is obtained by matching the virtual disk thrust to the calculated total resistance. The propeller revolutions are calculated based on the required thrust, inflow speed and open water curves.

Predictions which do not account for the hull surface roughness can significantly underestimate the delivered power [23]. Therefore, the surface roughness effect is incorporated through modification of the wall functions, using the roughness function based on the equivalent sand-grain roughness height. This approach is described in detail in the work of Mikkelsen and Walther [24]. The same method was successfully implemented in the studies of Farkas et al. [25-26]. An equivalent sand-grain roughness value of 30 μm is applied, according to the measurements for the anti-fouling coating presented in [27].

To reduce the computational effort, geometric symmetry is used to model only one side of the vessel. Both inlet and outlet boundaries are placed at $2.25L_{WL}$ from the respective perpendiculars. Other domain extents are shown in Fig. 7.

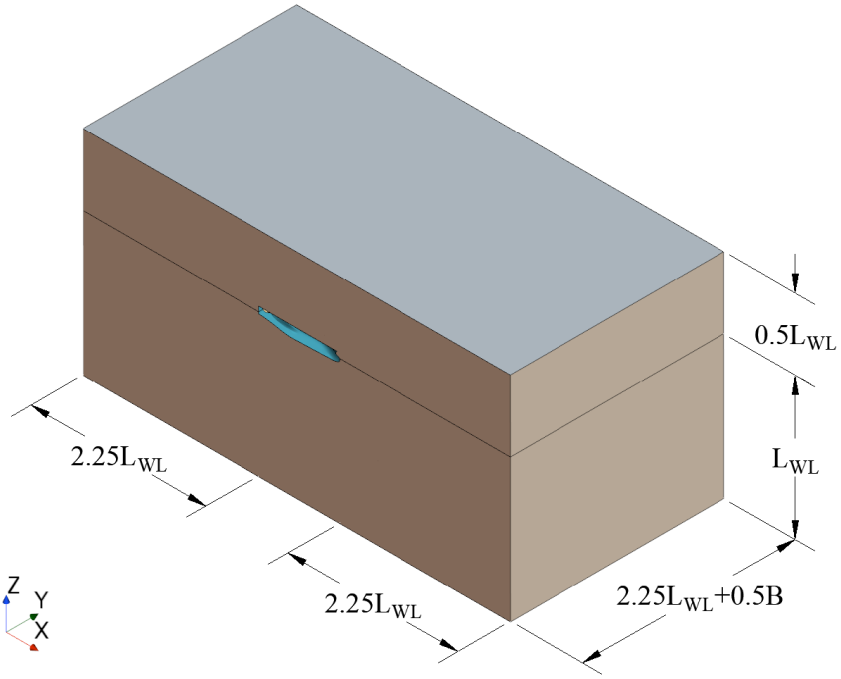

Fig. 7 Domain dimensions

The hull surface is set as a no-slip wall and symmetry condition is applied at the $X-Z$ midplane. The outlet boundary is assigned a pressure outlet condition, while the velocity inlet condition is applied to all other boundaries, as shown in Fig. 8. A VoF wave damping is applied at the inlet, outlet and far side boundaries to assure that results are not compromised by waves reflecting from the domain boundaries back to the vessel. At the beginning of a simulation, larger damping zone is used to ensure a faster convergence of the results [28]. As the simulation progresses, damping length is progressively decreased, with the final damping length value being $1.5L_{WL}$.

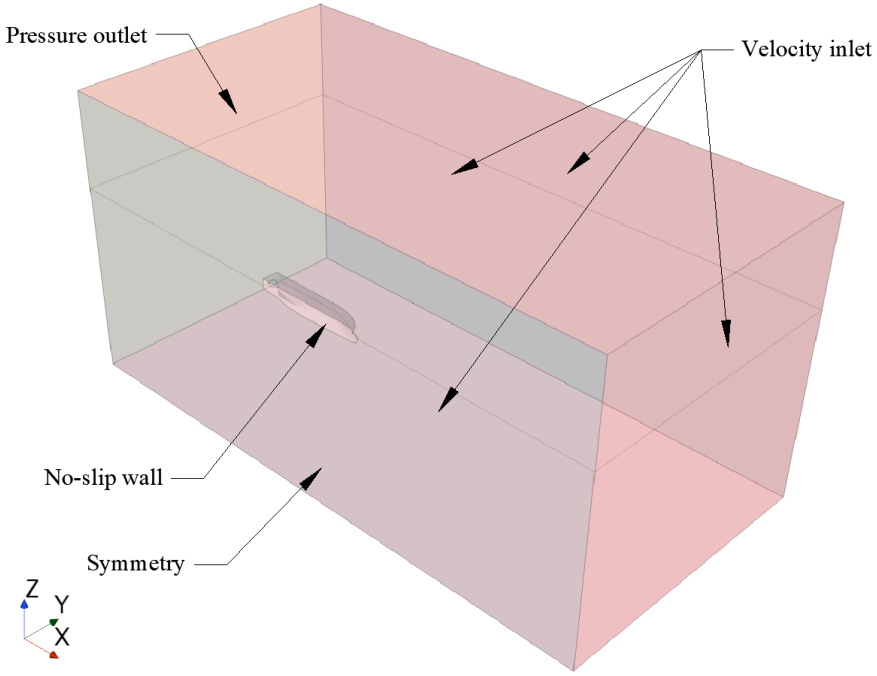

Fig. 8 Boundary conditions

An unstructured mesh with hexahedral cells is used to discretize the fluid domain. Several refinements zones are used around the bow, stern and skegs. Further refinements are made around the virtual disk and the free surface region. A side view of the volume mesh cross section ($y = 0$) is shown in Fig. 9 while a top view of the volume mesh cross section ($z = 0$), detailing the Kelvin wake refinement, is shown in Fig. 10. An example of the resulting wave pattern for the highest power setting and medium mesh and time-step sizes is shown in Fig**.** 11. The hull surface mesh in the bow and stern region is shown in Fig. 12 and Fig. 13, respectively. Prism cells are created on the hull surfaces, and a wall function is used. The prism cells are set to obtain y^+ values of around 100. All simulations were run on a 48-core workstation. When considering simulations with medium mesh size and medium time-step value, the total wall clock time ranged from 6.26 hours for lowest velocity to 14.11 hours for highest velocity.

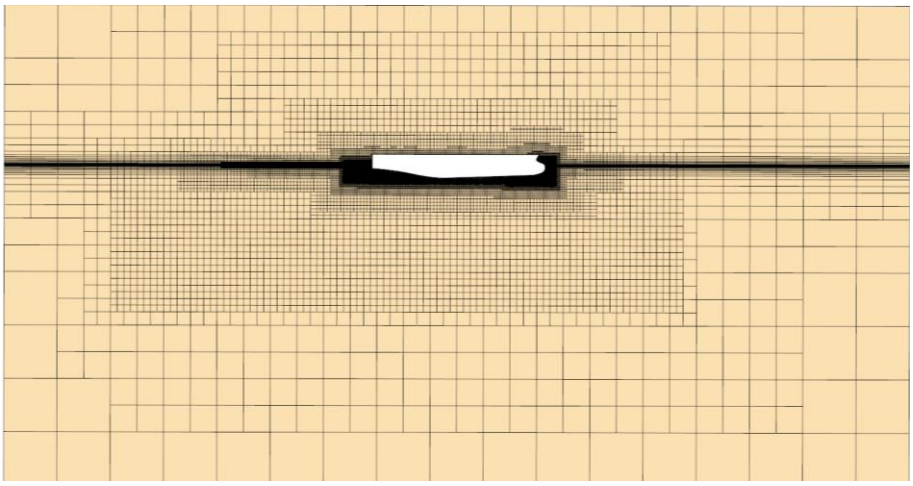

Fig. 9 Volume mesh side view

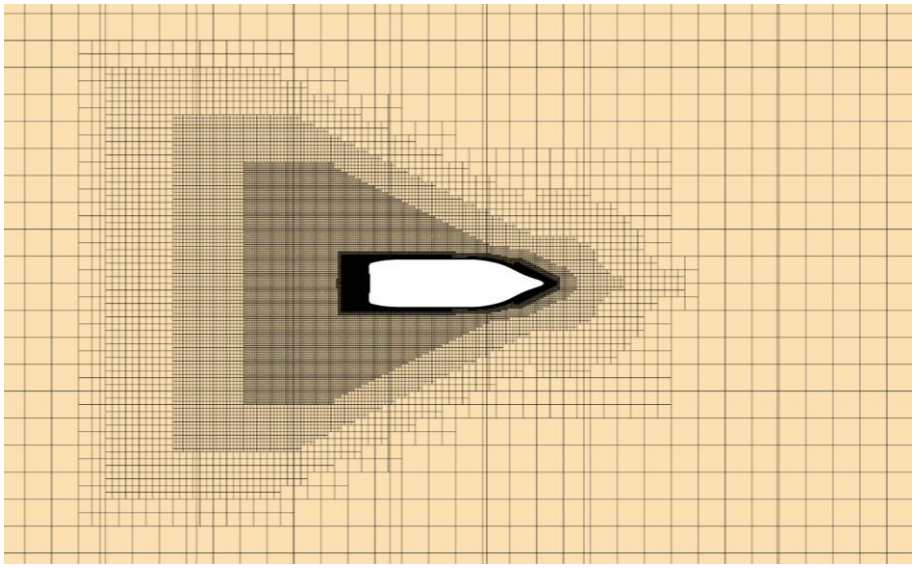

Fig. 10 Volume mesh top view

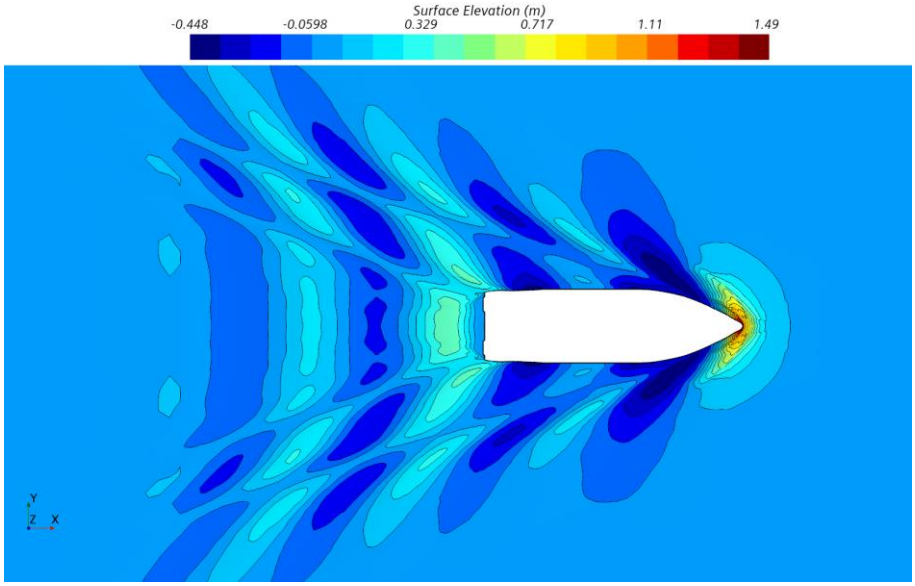

Fig. 11 Wave pattern - 77% power (medium mesh and time-step size)

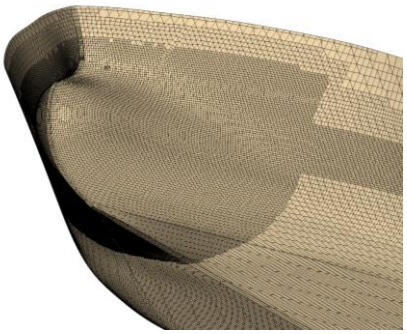

Fig. 12 Hull surface mesh (bow view)

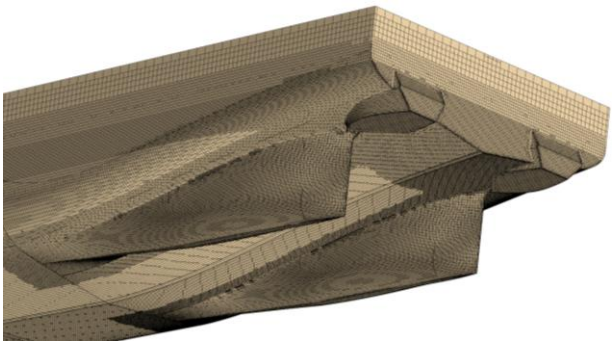

Fig. 13 Hull surface mesh (stern view)

4. Results

4.1 Azimuth thruster open water performance

As mentioned, thrust and torque coefficients are necessary for the virtual disk model to work. Due to the complexity of the installed thrusters, experimental data from model tests is unavailable. Therefore, full-scale open water CFD simulations were conducted to determine the open water coefficients. As mentioned previously, the propeller rotation was modelled using the Moving Reference Frame (MRF) method. This method comes with a significantly lower computational cost when compared to the rigid body motion method [29]. Seven steady-state simulations with constant propeller revolutions were conducted for the advance coefficient values between 0.1 and 1.3. The fluid domain was discretized using approximately 10 million hexahedral cells. No investigation was conducted to determine grid sensitivity in this case. Contributions from both nozzle and propeller are included in the dimensionless coefficients which are shown in Fig. 14, with $K_T = \mathrm{T}/(\rho n^2 D^4)$ being thrust coefficient, $K_Q = \mathrm{Q}/(\rho n^2 D^5)$ being torque coefficient and efficiency expressed as $\eta_0 = JK_T/(2\pi K_Q)$.

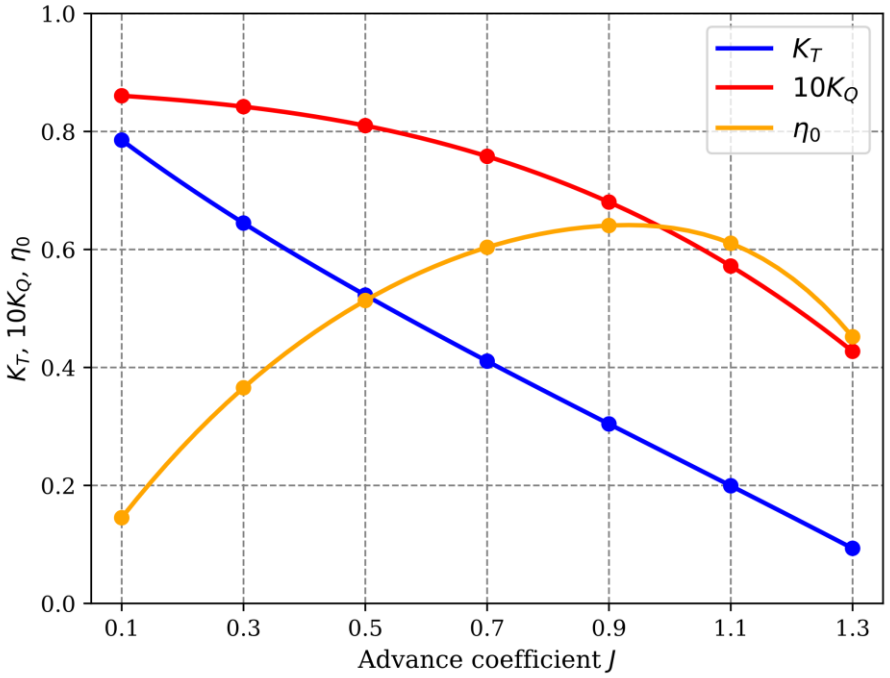

Fig. 14 Azimuth open water coefficients

4.2 Verification

The verification study with respect to grid size and time step is performed for self-propulsion simulations for each power setting. Discretization errors for total resistance R_T and propeller revolutions n are estimated using the Grid Convergence Index (GCI) method, as presented in [1]. Three distinctively different meshes were created for each power setting with representative grid size ratios greater than 1.3, as recommended in [1]. In addition to the number of cells N and representative grid size h, grid size ratios r_i are presented in Table 6. Values affiliated with coarse, medium, and fine mesh are denoted with 3, 2 and 1, respectively.

Table 6 Grid properties

Power, %	Coarse		Medium		Fine		r_i
	$N_3 \cdot 10^6$	h_3, m	$N_2 \cdot 10^6$	h_2, m	$N_3 \cdot 10^6$	h_1, m	
77	2.15	0.900	4.97	0.680	11.52	0.514	1.32
60	1.97	0.935	4.37	0.717	9.66	0.550	1.30
40	1.75	0.962	4.08	0.726	9.56	0.547	1.33

Once a solution is obtained on each selected grid, the apparent order p of the method is calculated using the following three expressions:

$$p = \frac{1}{\ln(r_{21})} |\ln|\varepsilon_{32}/\varepsilon_{21}| + q(p)| \tag{16}$$

$$q(p) = \ln\left(\frac{r_{21}^p - s}{r_{32}^p - s}\right) \tag{17}$$

$$s = \text{sgn}(\varepsilon_{32}/\varepsilon_{21}) \tag{18}$$

Where ε_{32} is the difference between the solutions obtained from coarse and medium grids and ε_{21} is the difference between solutions obtained from medium and fine grids. Using the apparent order p, extrapolated solution is calculated using the following term:

$$\phi_0 = (r_{21}^p \phi_1 - \phi_2)/(r_{21}^p - 1) \tag{19}$$

Finally, approximate relative error, extrapolated relative error and the fine-grid convergence index are calculated using the respective formulae:

$$e_a^{21} = \left|\frac{\phi_1 - \phi_2}{\phi_1}\right| \tag{20}$$

$$e_{ext}^{21} = \left|\frac{\phi_0 - \phi_1}{\phi_0}\right| \tag{21}$$

$$GCI = \frac{1.25 e_a^{21}}{r_{21}^p - 1} \tag{22}$$

Using the procedure described above, approximate relative error, extrapolated relative error, and the fine-grid convergence index is calculated for total resistance and propeller revolutions. In addition to these values, apparent order p and extrapolated solution for an ideal mesh ϕ_0 are reported in Table 7, 8 and 9. Following the formulation of convergence and divergence types presented in [30], divergence is achieved for the highest power setting, as illustrated in Fig. 15. On the other hand, results for medium and low power setting exhibit monotonic behaviour, as visualized in Fig. 16 and Fig. 17. A somewhat higher uncertainty is obtained for the total resistance at the highest power setting, with a GCI value of 4.52%. At the same time, a practically insignificant uncertainty is achieved for the propeller revolutions. Medium power setting results show more consistent values, with relatively low GCI values of 1.62% and 1.84% for total resistance and propeller revolutions, respectively. Finally, an even lower uncertainty is achieved for the lowest power settings, with grid convergence indices under 1% for both values of interest.

Table 7 Mesh sensitivity results for 77% power

77% Power	ϕ_3	ϕ_2	ϕ_1	ϕ_0	p	e_a^{21}, %	e_{ext}^{21}, %	GCI, %
R_T, kN	20.57	20.34	20.01	19.28	1.37	1.67	3.75	4.52
n, min^{-1}	158.9	158.5	157.7	156.9	2.50	0.51	0.51	0.63

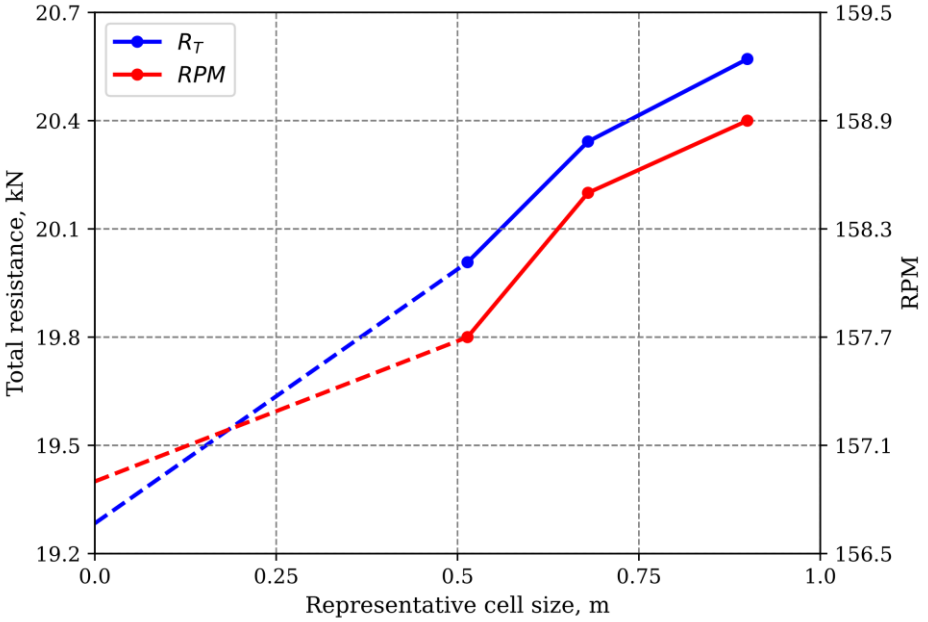

Fig. 15 Mesh sensitivity results for 77% power

Table 8 Mesh sensitivity results for 60% power

60% Power	ϕ_3	ϕ_2	ϕ_1	ϕ_0	p	e_a^{21}, %	e_{ext}^{21}, %	GCI, %
R_T, kN	11.81	11.46	11.3	11.15	2.87	1.46	1.31	1.62
n, min^{-1}	123.6	122.8	122.2	120.4	1.10	0.49	1.50	1.84

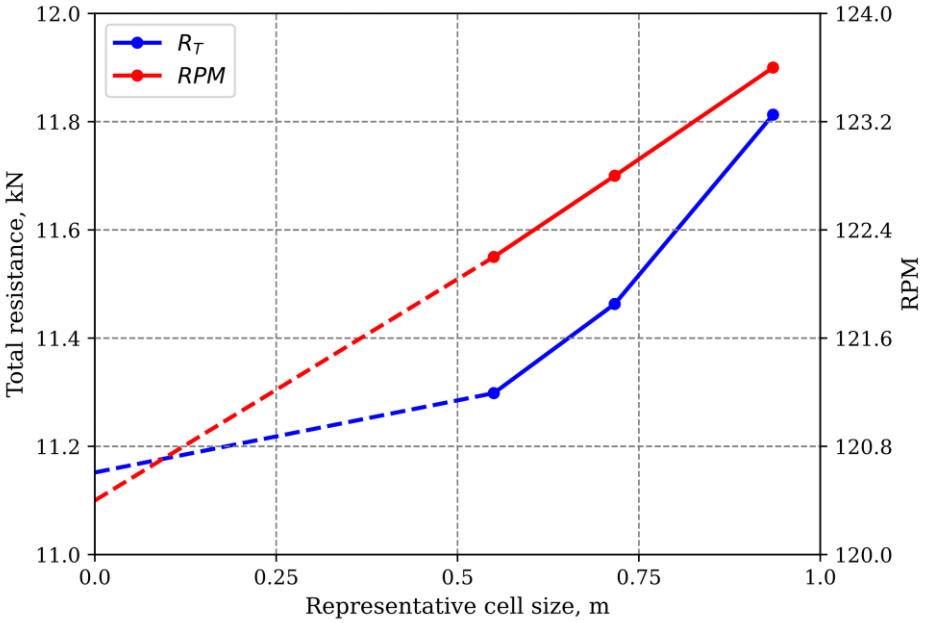

Fig. 16 Mesh sensitivity results for 60% power

Table 9 Mesh sensitivity results for 40% power

40% Power	ϕ_3	ϕ_2	ϕ_1	ϕ_0	p	e_a^{21}, %	e_{ext}^{21}, %	GCI, %
R_T, kN	3.43	3.29	3.25	3.22	3.79	1.42	0.73	0.91
n, min^{-1}	70.1	69.5	69.2	68.9	2.43	0.43	0.44	0.54

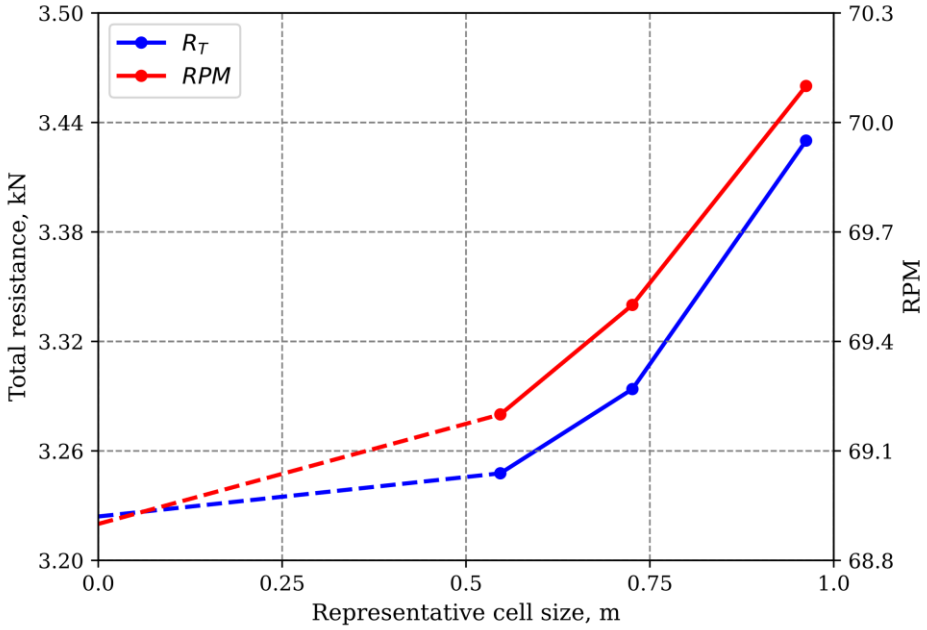

Fig. 17 Mesh sensitivity results for 40% power

As a compromise between accuracy and calculation time, a medium grid size was used for all power settings in the time-step sensitivity analysis. According to the ITTC recommendations [31], a time-step value in the range of 0.005 ~ 0.01 L/v should be used, where L is the ship's length and v is the ship's velocity. The lowest value in this range was chosen for the initial simulations used in the mesh study. Consequently, this time step was considered the medium value in the time step sensitivity study. For the coarse and fine time steps, values of $0.01L/v$ and $0.0025L/v$ are chosen, respectively. This results in a refinement ratio of two. As with the grid sensitivity study, the uncertainty is calculated for total resistance and propeller revolutions across all power settings. As shown in Table 10, monotonic convergence is obtained for 77% power case. Further, low uncertainty is observed, with GCI values being 0.25% for resistance and 0.06% for propeller revolutions.

Table 10 Time step sensitivity for 77% power

77% Power	ϕ_3	ϕ_2	ϕ_1	ϕ_0	p	e_a^{21}, %	e_{ext}^{21}, %	GCI, %
R_T, kN	20.3	20.34	20.75	20.8	3.45	1.99	0.20	0.25
n, min^{-1}	158.41	158.48	159.39	159.46	3.72	0.57	0.05	0.06

At the same time, oscillatory convergence is achieved for 60% and 40% power. In cases when oscillatory convergence is obtained, calculations with at least two additional refinements should be performed to assess uncertainty values. Since this would require a significant amount of computational effort, a simplified approach proposed by [32] is used to evaluate uncertainty:

$$U = 0.5F_S(\phi_{max} - \phi_{min}) \tag{23}$$

Where $F_S = 3$ is the safety factor while ϕ_{max} and ϕ_{min} represent maximum and minimum values obtained for three different time-steps. The numerical uncertainties calculated using this approach are presented in Table 11 and Table 12. For the medium power setting, an uncertainty of 0.02 kN or 0.16% of the fine time step solution was calculated for resistance. Further, uncertainty of 0.16 min^{-1} or 0.13% of the fine solution is achieved for the propeller revolutions. Slightly larger uncertainty is observed at the 40% power setting for the total resistance, with uncertainty values of 1.35% and 0.36% for total resistance and propeller revolutions, respectively.

Table 11 Time step sensitivity for 60% power

60% Power	ϕ_3	ϕ_2	ϕ_1	r_i	U	U, %
R_T, kN	11.47	11.46	11.48	2.0	0.02	0.16
n, min^{-1}	122.78	122.82	122.72		0.16	0.13

Table 12 Time step sensitivity for 40% power

40% Power	ϕ_3	ϕ_2	ϕ_1	r_i	U	U, %
R_T, kN	3.32	3.29	3.30	2.0	0.04	1.35
n, min^{-1}	69.64	69.47	69.49		0.25	0.36

To verify that the assumptions regarding the turbulence model and symmetry condition are valid, additional simulations were conducted using medium grid size and medium time step values. Simulations were set up using the $k-\omega\ SST$ model, to investigate the effect of the turbulence model. All other aspects of the numerical setup remained unchanged. Table 13 presents the total resistance and propeller revolutions obtained with the $k-\omega\ SST$ turbulence model and their difference from the values obtained with the $k-\varepsilon$ model. It can be concluded that the turbulence model does not have a significant impact on the results.

Table 13 Impact of the turbulence model on simulation results

V_S, kn	R_T, kN		n, min^{-1}		ΔR_T, %	Δn, %
	$k-\varepsilon$	$k-\omega\ SST$	$k-\varepsilon$	$k-\omega\ SST$		
10.53	20.34	20.14	158.5	158.1	-0.98	-0.25
8.46	11.46	11.36	122.8	122.2	-0.87	-0.49
5.02	3.29	3.31	69.5	69.6	0.61	0.14

Further, to confirm the premise that there is no significant interaction between the port and sideboard azimuth thrusters and that only half of the domain can be modelled, full-domain simulations were conducted for the three power settings. As previously mentioned, medium grid side and medium time step values were used while all other parameters remained constant. Table 14 presents results obtained from full domain simulations and their difference with respect to the values from the half domain simulations. Note that half of the total resistance is shown for the full domain value. Propeller revolutions are shown for both the port and the starboard azimuth thrusters and their average value is compared to the half domain value. However, observed differences were so insignificant that they are not visible after rounding. These results confirm that modelling only one side of the ship is a valid approach in this case.

Table 14 Impact of the symmetry condition on simulation results

V_S, kn	R_T, kN		n, min^{-1}			ΔR_T, %	Δn, %
			Half domain	Full domain			
	Half domain	Full domain		Port	Starboard		
10.53	20.34	20.36	158.5	158.5	158.5	0.10	0.00
8.46	11.46	11.45	122.8	122.7	122.7	-0.09	-0.08
5.02	3.29	3.3	69.5	69.5	69.5	0.30	0.00

4.3 Validation

Results of simulations with medium grid and time-step sizes are compared with the corrected trial data. To calculate the delivered power from the CFD simulation results, the quasi-propulsive efficiency must be calculated:

$$\eta_{\mathrm{D}} = \eta_H \eta_R \eta_0 \tag{24}$$

Where η_H is the hull efficiency, η_R is the relative rotative efficiency and η_0 is the thruster open water efficiency. Open water efficiency is obtained from the open water performance curves for the obtained advance coefficient. Relative rotative efficiency can be calculated from the self-propulsion results using the following expression:

$$\eta_R = \frac{K_{Q0}}{K_{QS}} \tag{25}$$

Where K_{QS} is the torque coefficient from the self-propulsion simulation and K_{Q0} is the torque coefficient obtained from the open water performance curves for the same advance coefficient. Finally, hull efficiency is calculated based on the thrust deduction factor t and wake fraction w using the following term:

$$\eta_R = \frac{1-t}{1-w} \tag{26}$$

To obtain the thrust deduction factor t, additional resistance simulations were performed. In these simulations, an identical setup to the self-propulsion simulations was used, however, without the presence of the virtual disk. Medium values were used for both the grid and time-step size. All the described efficiency factors, along with thrust deduction and wake fraction are presented in Table 15.

Table 15 Propulsion efficiency

V, kn	t	w	η_H	η_R	η_0	η_{D}
10.53	0.070	0.013	0.942	1.048	0.622	0.615
8.46	0.064	0.026	0.961	1.001	0.614	0.591
5.02	0.059	0.037	0.977	1.004	0.597	0.587

Validation results for propeller revolutions and delivered power are shown in Table 16. Propeller revolution values obtained from the simulations are in good agreement with the corrected trial measurements. Generally, simulation results under predict propeller revolutions, with a relative error of -2.70% for the highest power setting, -2.46% for the medium power and -4.40% for the lowest power setting. However, significant discrepancies are observed when comparing delivered power values. Relative errors range from -30.15% for the medium velocity to -41.93% for the lowest velocity.

Table 16 Validation of propeller revolutions and delivered power

V, kn	n_{corr}, min^{-1}	n_{CFD}, min^{-1}	Δn, %	$P_{D,corr}$, kW	$P_{D,CFD}$, kW	ΔP_D, %
10.53	162.9	158.5	-2.70	525.07	358.46	-31.73
8.46	125.9	122.8	-2.46	241.57	168.73	-30.15
5.02	72.7	69.5	-4.40	49.94	29.00	-41.93

A significant part of these errors can be attributed to insufficient understanding of the logging system installed onboard the vessel. As mentioned in the trial description, the ship was operating at reduced power on the day of the trial. Since the power delivered to each azimuth thruster is calculated rather than measured, it is unknown to the authors how the reduced engine output is reflected in this. In an attempt to address this, corrected power values were reduced to 77% of the original value, according to the maximum available power during the trial. These tentative values are presented in Table 17. A significant reduction in error is observed for the tentative results, which suggests that this is a plausible explanation for the large differences between simulated and corrected delivered power. At the highest power setting, CFD underpredicts delivered power by -10.71%, while the lowest error of -8.52% is again obtained for the medium power setting. Finally, a relatively large error of -23.08 persists in the case of the lowest power setting. Relatively larger errors for the lowest power setting are expected, as no correction was made for the added resistance due to waves since available methods were not applicable for the encountered wave conditions. Tentative power values, alongside corrected trial and simulation results, are visualized in Fig. 18.

Table 17 Tentative delivered power

V, kn	$P_{D,tentative}$, kW	$P_{D,CFD}$, kW	ΔP_D, %
10.53	401.45	358.46	-10.71
8.46	184.44	168.73	-8.52
5.02	37.7	29.00	-23.08

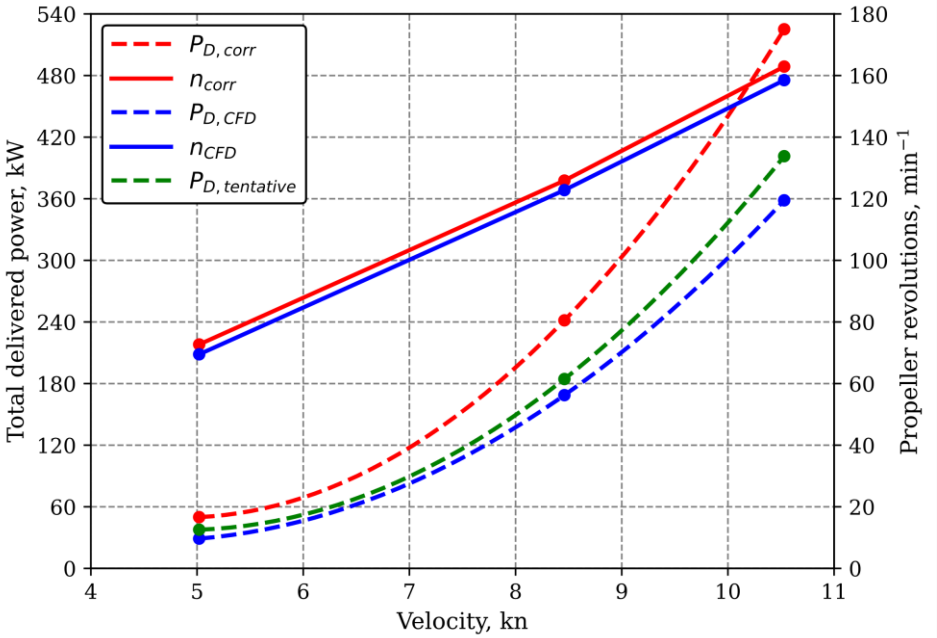

Fig. 18 Validation results

5. Conclusion

An extensive verification and validation study of ship scale CFD self-propulsion simulations is presented. As a part of the study, a speed/power sea trial was conducted with a research vessel for three different power settings. Results were analysed and corrected to account for the encountered environmental conditions according to the ITTC procedures.

Viscous flow around the ship in full scale was modelled with RANS equations for a transient, incompressible, free surface flow. Azimuth thruster was modelled using the virtual disk method to reduce the computation time. Numerical uncertainties due to the finite number of cells were assessed according to the GCI method. Relatively low uncertainty values were observed, ranging from 0.54% to 4.52%. Further, the solution sensitivity to time step was evaluated. Negligible values were observed in most cases, ranging from 0.06% to 1.35%. Since propulsion coefficients such as wake fraction and thrust deduction are virtually impossible to measure in full scale, only propeller revolutions and delivered power values were validated.

Propeller revolution values showed good agreement with the trial data, and relative errors compared to the corrected trial data ranged from -2.46% to -4.40%. On the other hand, considerably higher errors were observed when comparing delivered power values, ranging from -30.15% to -41.93%. These uncharacteristically high differences can be partly attributed to the insufficient knowledge about the installed logging system on the vessel and how the delivered power is calculated. Tentative values are provided, which try to account for the reduced engine input during the sea trial. When comparing CFD results with these values, significantly lower errors are observed, ranging from -8.52% to -23.08%. As expected, the most significant errors were obtained for the 40% power setting since no correction was made for the wave-added resistance for that case. In general, the tendency of CFD to underpredict both propeller revolutions and delivered power is observed.

Verification and validation results showed very good results when considering propeller revolution values. Results for the delivered power showed more considerable discrepancies. In addition to the uncertainties of the numerical model, these large errors can be partly explained by the aforementioned issues with the sea trial data. Furthermore, replacing the azimuth thrusters with virtual disks has a more significant impact on the power results as the interaction between the hull, nozzle and propeller is not captured. This can affect the propulsive coefficients and consequently, the propeller delivered power. This assumption should be investigated as a part of future work by comparing virtual disk model with a fully discretized azimuth thruster. Based on the obtained propeller revolutions, it can be concluded that the study showed promising results and highlighted the capabilities of CFD in investigating and predicting ship performance at full scale.

REFERENCES

[1] Celik, I. B., Ghia, U., Roache, P. J., Freitas, C. J., Coleman, H., Raad, P. E., 2008. Procedure for Estimation and Reporting of Uncertainty Due to Discretization in CFD Applications. *Journal of fluids engineering*, 130(7), 0780011-0780014. https://doi.org/10.1115/1.2960953

[2] ITTC, 2021. Recommended Procedures and Guidelines, 1978 ITTC Performance Prediction Method 7.5-02-03-01.4.

[3] Hochkirch, K., Mallol, B., 2013. On the importance of full-scale CFD simulations for ships. *12th International conference on computer and IT applications in the maritime industries*, Cortona, Italy.

[4] Castro, A. M., Carrica, P. M.,Stern, F., 2011. Full scale self-propulsion computations using discretized propeller for the KRISO container ship KCS. *Computers & fluids*, 51(1), 35-47. https://doi.org/10.1016/j.compfluid.2011.07.005

[5] Farkas, A., Degiuli, N., Martić, I., Dejhalla, R., 2018. Numerical and experimental assessment of nominal wake for a bulk carrier. *Journal of marine science and technology*, 24(4), 1092-1104. https://doi.org/10.1007/s00773-018-0609-4

[6] Visonneau, M., Deng, G., Guilmineau, E., Queutey, P.,Wackers, J., 2016. Local and global assessment of the flow around the Japan bulk carrier with and without energy saving devices at model and full scale. *31st Symposium on Naval Hydrodynamics*, Monterey, California, USA.

[7] Farkas, A., Degiuli, N., Martić, I., 2018. Assessment of hydrodynamic characteristics of a full-scale ship at different draughts. *Ocean Engineering*, 156, 135-152. https://doi.org/10.1016/j.oceaneng.2018.03.002

[8] Niklas, K.,Pruszko, H., 2019. Full-scale CFD simulations for the determination of ship resistance as a rational, alternative method to towing tank experiments. *Ocean engineering*, 190, 106435. https://doi.org/10.1016/j.oceaneng.2019.106435

[9] Lloyd's Register, 2016. Workshop on Ship Scale Hydrodynamic Computer Simulation. https://www.lr.org/en/latest-news/worlds-first-full-scale-numerical-modelling-workshop-facilitated-by-lloyds-register/. accessed 1st August 2022.

[10] Ponkratov, D., Zegos, C., 2015. Validation of ship scale CFD self-propulsion simulation by the direct comparison with sea trials results. *Fourth International Symposium on Marine Propulsors*, Austin, Texas, USA.

[11] Jasak, H., Vukčević, V., Gatin, I., Lalović, I., 2019. CFD validation and grid sensitivity studies of full scale ship self propulsion. *International Journal of Naval Architecture and Ocean Engineering*, 11(1), 33-43. https://doi.org/10.1016/j.ijnaoe.2017.12.004

[12] Orych, M., Werner, S., Larsson, L., 2021. Validation of full-scale delivered power CFD simulations. *Ocean Engineering*, 238, 109654. https://doi.org/10.1016/j.oceaneng.2021.109654

[13] ITTC, 2021. Recommended Procedures and Guidelines, Preparation, Conduct and Analysis of Speed/Power Trials 7.5-04-01-01.1.

[14] Degiuli, N., Farkas, A., Martić, I., Zeman, I., Ruggiero, V., Vasiljević, V., 2021. Numerical and experimental assessment of the total resistance of a yacht. *Brodogradnja*, 72(3), 61-80. https://doi.org/10.21278/brod72305

[15] Que´rard, A., Temarel, P., Turnock, S. R., 2008. Influence of Viscous Effects on the Hydrodynamics of Ship-Like Sections Undergoing Symmetric and Anti-Symmetric Motions, Using RANS. *27th International Conference on Offshore Mechanics and Arctic Engineering*, Estoril, Portugal. https://doi.org/10.1115/omae2008-57330

[16] van den Boom, H., Huisman, H., Mennen, F., 2013. New guidelines for speed/power trials: Level playing field established for IMO EEDI. *SWZ|Maritime*, 1-11.

[17] STA-Group, 2021. STAIMO. https://www.staimo.com/. accessed 1st August 2022.

[18] Ferziger, J. H., Perić, M., Street, R. L., 2020. Computational methods for fluid dynamics. *Springer*, Cham, Switzerland. https://doi.org/10.1007/978-3-319-99693-6

[19] Siemens Digital Industries Software, 2022. Simcenter STAR-CCM+ User Guide V16.06.

[20] Goldstein, S., 1929. On the vortex theory of screw propellers. *Proceedings of the Royal Society of London. Series A, Containing Papers of a Mathematical and Physical Character*, 123(792), 440-465. https://doi.org/10.1098/rspa.1929.0078

[21] Tezdogan, T., Demirel, Y. K., Kellett, P., Khorasanchi, M., Incecik, A., Turan, O., 2015. Full-scale unsteady RANS CFD simulations of ship behaviour and performance in head seas due to slow steaming. *Ocean Engineering*, 97, 186-206. https://doi.org/10.1016/j.oceaneng.2015.01.011

[22] Dai, K., Li, Y., Gong, J., Fu, Z., Li, A.,Zhang, D., 2022. Numerical study on propulsive factors in regular head and oblique waves. *Brodogradnja*, 73(1), 37-56. https://doi.org/10.21278/brod73103

[23] Sun, W., Hu, Q., Hu, S., Su, J., Xu, J., Wei, J., Huang, G., 2020. Numerical analysis of full-scale ship self-propulsion performance with direct comparison to statistical sea trail results. *Journal of marine science and engineering*, 8(1), 24. https://doi.org/10.3390/jmse8010024

[24] Mikkelsen, H., Walther, J. H., 2020. Effect of roughness in full-scale validation of a CFD model of self-propelled ships. *Applied ocean research*, 99, 102162-14. https://doi.org/10.1016/j.apor.2020.102162

[25] Farkas, A., Degiuli, N., Martić, I., 2018. Towards the prediction of the effect of biofilm on the ship resistance using CFD. *Ocean Engineering*, 167, 169-186. https://doi.org/10.1016/j.oceaneng.2018.08.055

[26] Farkas, A., Song, S., Degiuli, N., Martić, I., Demirel, Y. K., 2020. Impact of biofilm on the ship propulsion characteristics and the speed reduction. *Ocean Engineering*, 199, 107033. https://doi.org/10.1016/j.oceaneng.2020.107033

[27] Schultz, M. P., 2007. Effects of coating roughness and biofouling on ship resistance and powering. *Biofouling*, 23(5), 331-341. https://doi.org/10.1080/08927010701461974

[28] Farkas, A., Degiuli, N., Martić, I., 2017. Numerical simulation of viscous flow around a tanker model. *Brodogradnja*, 68(2), 109-125. https://doi.org/10.21278/brod68208

[29] Dogrul, A., 2022. Numerical prediction of scale effects on the propulsion performance of Joubert BB2 submarine. *Brodogradnja*, 73(2), 17-42. https://doi.org/10.21278/brod73202

[30] Eça, L., Hoekstra, M., 2014. A procedure for the estimation of the numerical uncertainty of CFD calculations based on grid refinement studies. *Journal of computational physics*, 262, 104-130. https://doi.org/10.1016/j.jcp.2014.01.006

[31] ITTC, 2011. Recommended Procedures and Guidelines, Practical Guidelines for Ship CFD Application, 7.5-03-02-03.

[32] Stern, F., Wilson, R. V., Coleman, H. W., Paterson, E. G., 2001. Comprehensive approach to verification and validation of CFD simulations—part 1: methodology and procedures. *Journal of Fluids Engineering*, 123(4), 793-802. https://doi.org/10.1115/1.1412235

Submitted: 27.09.2022.
Accepted: 20.12.2022.

Marko Mikulec, marko.mikulec@ntnu.no
Henry Piehl
Norwegian University of Science and Technology,
Department of Ocean Operations and Civil Engineering,
Larsgaardsvegen 2, Aalesund, Norway